A&A 383, 614–630 (2002)
DOI: 10.1051/0004-6361:20011766

Astronomy & Astrophysics

VLBI observations of 6.7 and 12.2 GHz methanol masers toward high mass star-forming regions

III. The milliarcsecond structures of masing regions

V. Minier[1,2], R. S. Booth[1], and J. E. Conway[1]

[1] Onsala Space Observatory, 439 92 Onsala, Sweden
[2] Department of Astrophysics and Optics, School of Physics, University of New South Wales, NSW 2052, Australia

Received 20 September 2001 / Accepted 5 December 2001

Abstract. We consider the milliarsecond scale structures of three representative methanol maser sites observed at high resolution with the EVN at 6.7 GHz and with the VLBA at 12.2 GHz. These observations suggest that the majority of the individual masing regions within a maser site consist of a compact core surrounded by extended emission, i.e. a core/halo structure. In many cases, the extended emission is resolved by the shortest baselines of the VLBA. We conclude that these regions of extended emission are responsible for the missing flux density when comparing cross-power spectra on the shortest VLBI baselines to single dish spectra. The halos of diffuse emission have diameters ranging between 12 and 290 AU and their brightness temperatures depend on their diameters as $T_{\rm b} \propto d^{-2.2}$. The core diameters vary from 2 to 20 AU. Three possible phenomena could explain the presence of large halos around bright cores. The core/halo pattern could be the result of saturation effects in a uniform spherical maser cloud. The compact and diffuse masers could also originate in physically distinct regions: the maser core could form within highly dense gas while the maser halo could be the result of weak masers in diffuse gas. Finally, turbulence could cause the appearance of core/halo structures in a disrupted homogeneous medium. Scattering effects do not seem to play a role in the broadening of maser images since masers have similar sizes at 6.7 and 12.2 GHz.

Key words. masers – stars: formation – circumstellar matter – techniques: interferometric

1. Introduction

Individual masing regions are frequently described as "spots" in the literature on VLBI observations of OH, H_2O, SiO and CH_3OH masers, because their angular dimensions are reported to be comparable or smaller than a synthesised beam with a diameter of a few milliarcseconds. The masing regions are therefore believed to be very compact structures, and their dimensions are important parameters in the modelling of maser radiation. Indeed, the dimensions of maser spots measured by VLBI techniques can be used to derive brightness temperatures from observed peak emission in cleaned VLBI images. For example, Sobolev et al. (1997a) built their model of 6.7 GHz methanol masers in order to reproduce the results of VLBI observations in W 3(OH) by Menten et al. (1992) who found maser spot sizes below 2 mas and $T_{\rm b} = 3 \times 10^{12}$ K. The study of the individual masing regions is therefore crucial in order to better constrain maser models.

The present paper focuses on studying the detailed structures of methanol masing regions within three representative methanol maser sites. Unlike the H_2O, SiO and OH masers extensively studied at high resolution, only the 6.7 and 12.2 GHz methanol masers in W 3(OH) had been imaged in the Northern hemisphere using VLBI observations (Menten et al. 1988, 1992; Moscadelli et al. 1999). Thus, milliarcsecond resolution observations of methanol masers were conspicuously lacking until recent observations by the Onsala group (e.g. Minier et al. 2000). In this sample, fifteen methanol maser sites have been imaged using the EVN at 6.7 GHz and the VLBA at 12.2 GHz. The overall morphologies of the methanol maser sites are described in Minier et al. (2000, hereafter Paper I). Paper I concentrated on finding the centroids of different velocity components and on describing the overall distribution of these components. The size and extent of each

Send offprint requests to: V. Minier,
e-mail: vminier@bat.phys.unsw.edu.au

Table 1. Studied methanol maser sources selected from Papers I and II. The overall size is the linear dimension of the maser distribution across the map as seen in Paper I. UC H II means ultra-compact H II region. MP stands for massive protostar.

Source	Overall size (AU)	Association	Exciting (proto)star
G 29.95–0.02	85	Hot core	MP
NGC 7538	1600	Outflow	O9
G 9.62+0.20	700	UC H II	B1

Table 2. Comparison of the peak flux densities of brightest spectral features in the VLBA total power spectra and previous single dish spectra. Single dish fluxes are taken from Caswell et al. (1995b) and Koo et al. (1988). The flux variability is given in Col. 6

Source	Single dish		VLBA		Variab.
	F(Jy)	Epoch	F(Jy)	Epoch	(%)
G 29.95-0.02	53	1992	70	1999	+32
NGC 7538	198	1986	125	1998	−36
G 9.62+0.20	180	1993	140	1998	−22

velocity component were not considered. In a second paper Minier et al. (2001, hereafter Paper II) investigated the likely association between young stellar objects and methanol maser sources. For the present paper, we concentrate on the detailed structure of each maser velocity component in three sources from Paper I. These three sources have been selected to be representative of the different observed morphologies. We have argued (Paper II) that these sources represent three different stages in the evolution of methanol masers within the process of massive star formation. The source names, the overall sizes of the maser sites and the associated stellar objects are listed in Table 1.

2. Gaussian fitting of visibility plots

For each of these methanol maser sources, four sets of data are presented:

1. The VLBI map of maser averaged-velocity components from Paper I (hereafter referred to as the VLBI centroid map);
2. The velocity integrated intensity images over the velocity width of spectral features (hereafter referred to as the intensity images);
3. The cross-power spectrum taken on the shortest VLBA baseline (Los Alamos-Pie Town: 236 km) and the total power spectrum on the Los Alamos antenna deduced from the VLBA auto-correlation functions;
4. The visibility vs. uv-distance plots for the channel corresponding to the peak intensity of each spectral feature (the visibility plots are presented in Appendix A).

In this paper we concentrate on the 12.2 GHz VLBA observations taken on the VLBA telescopes (10 antennas) because the amplitude calibration of both the total power and cross-power spectra are believed to be more accurate than those at 6.7 GHz using the EVN telescopes (5 antennas). Incomplete knowledge of the EVN antenna gains and system temperature made calibration uncertain. In addition it was not possible to derive accurate calibration at 6.7 GHz using the auto-correlation functions. This occurs because the EVN data were recorded in MkIV data format and correlated at the Socorro VLBA correlator. Then, because of slight inconsistencies in data format, the auto-correlation powers do not have reliable amplitudes. This is not the case for the VLBA data at 12.2 GHz where the auto-correlation function on each antenna could be used to produce highly accurate calibration. In addition to reliable amplitude calibration, the VLBA offers a wider range of projected baseline spacing from ∼6 to 170 megawavelengths (Mλ). The shortest and largest EVN baselines at 6.7 GHz correspond to projected uv distances of 9 and 30 Mλ, respectively. Thus, the visibility amplitude vs. uv-distance plots of the VLBA data give a more complete description of the visibility amplitude behaviour than those of the EVN data. Because of these advantages this study concentrates on 12 GHz data, however the 6.7 GHz data are used to confirm the nature of the unveiled structures that are seen at both transitions.

A comparison of the flux density taken on the VLBA antennas (total power spectra) with those measured using single dish techniques (Table 2) shows that flux densities have varied by 22 to 36%. The differences between flux densities in Table 2 could be explained by variability effects of maser radiation that frequently occurs in timescales of a few months to a few years in the case of methanol masers (e.g. Caswell et al. 1995a). Different frequency resolutions could also affect the comparison of the methanol maser spectra taken on different telescopes.

In the next sections, the visibility data for each of the selected maser sources are described. It is possible to get an estimate of the size of the structure by fitting Gaussian functions to the binned visibility amplitude vs. uv-distance. Assuming that Gaussian functions are convenient models for the source brightness, the visibility amplitudes can be fitted with Gaussian functions as well. It would also have been possible to directly estimate the scales by making maps and fitting to these. This gives an accurate estimate of the morphology of the detected emission but is a less reliable tracer of the very extended emission because much of the extended flux could be missing even on the shortest baselines. Instead, by Gaussian fitting the visibility amplitude and taking the value of the uv-distance ($uv = \sqrt{u^2 + v^2}$) corresponding to the half maximum amplitude, it is possible to estimate the size of a source (d) by using the relationship $uv = 2\ln 2/\pi d$ or if d is in arcsec and uv in wavelength, $d \simeq 91\,000/uv$. Note that only lower limits of the structure size can be set when only two points are used in Gaussian fitting. This will be indicated in the following tables.

2.1. G 29.95–0.02

Figure 1 shows the overall structures of the maser components in G 29.95–0.02. Each dot shows the averaged position over ∼0.2 km s^{-1} of the peak emission in the channel maps. The maser components are distributed along a line of 85 AU in extent in the VLBA centroid map. Figure 1 also shows that the amplitude of the cross-power spectrum on the shortest VLBA baseline is reduced compared to that of the total power spectrum. The spectrum consists of three features labelled A, B and C. The flux density of feature A is 45 Jy in the total power and 32 Jy in the cross-power spectrum. The reduction of flux is much more important for feature B where the peak flux density varies from 70 Jy to 45 Jy. Spectrally, the maser features in the total power spectrum are also slightly broader than those in the cross-power spectrum and feature C at 98.2 km s^{-1} has simply disappeared in the cross-power spectrum. These results indicate that the VLBA has resolved out some masing structures of which the flux density corresponds to the missing flux in the cross-power spectrum.

The intensity image in Fig. 1 supports the presence of extended emission resolved by the VLBA. By comparing the VLBA centroid map of maser components with the intensity image, it is striking that there is some extended emission linking the maser components. The maser components are not isolated and distinct spots, but they seem to be connected to each other by weaker emission. Moreover, weak emission (500 mJy beam^{-1} $\sim 10\sigma$) appears in the image NW to the original maser line.

Figure A.1 shows the visibility plots of two spectral channels corresponding to the maximum intensity of features A and B in the cross-power spectrum. The value at $uv = 0$ is taken from the total power spectrum. For both features A and B, the visibility amplitudes are reduced by ∼25 to 50% at the shortest baselines and are almost equal to zero at the longest baselines. These results suggest that the VLBA totally resolves the masing structures and that even the most compact part of the maser is bigger than the fringe spacing on the longest VLBA baseline (i.e. >1 mas). Additionally, the reduction of the visibility amplitude for feature B appears to occur in two steps. First, the visibility amplitude is reduced by a factor 2 at the shortest baseline, and then the correlated flux decreases more slowly from 30 to 0 Jy with the uv-distance. One possible explanation is that two structures with similar spectral properties are present at the same location. In such a case, it is possible to give a rough estimate of the sizes of masing structures by fitting the visibility amplitude for the channels corresponding to the maximum intensity of features A and B in the total power spectrum with two Gaussian functions. The Gaussian function fitting is shown in Fig. A.1 and the results are given in Table 3. The visibility amplitude of feature B is well fitted with two Gaussian functions and is probably produced by two structures: a compact structure of 20 AU in extent and an extended structure of >112 AU in extent. Since the visibility amplitude for B decreases by 50% in going from 0 to 6 Mλ, it is only possible to give a lower limit of its size. The visibility amplitude of feature A is fitted with only one Gaussian function. No extended emission is detected around the compact structure of 18 AU in extent.

2.2. NGC 7538

Figure 2 shows the VLBI centroid map of the 6.7 and 12.2 GHz masers in NGC 7538-IRS1. As argued in Minier et al. (1998), the methanol masers trace a probable disk (Group A) and the blue-shifted part of an outflow (Groups B, C, D, E). The group A is sub-divided into two structures A1 and A2. A2 is only seen at 6.7 GHz. Groups B, D, E are not detected at 12.2 GHz. Figure 2 also shows the total power and cross-power spectra at 12.2 GHz. The spectrum is dominated by two features labelled A and C which correspond to the groups A and C in the VLBI centroid map. On the baseline KP-OV (845 km), the feature A is spectrally resolved into three features that correspond in flux and LSR velocities to the knots 1, 2 and 3 in the intensity image of group A1 at 12.2 GHz. Furthermore, the flux density of feature A in the cross-power spectrum is significantly reduced on long baselines. A much larger reduction is also clearly visible for feature C. This missing flux at the longest baselines indicates that some extended emission is resolved by the VLBA.

The intensity image of A1 at 12.2 GHz (Fig. 2) clearly shows that the maser components are continuously distributed along an elongated structure. As a comparison, the intensity images of groups A1 and A2 at 6.7 GHz are also shown in Fig. 2. The synthesised beam of the EVN at 6.7 GHz is five times larger than that of the VLBA at 12.2 GHz. The observed group A1 is larger at 6.7 GHz than at 12.2 GHz. A possible explanation is that the VLBA resolves extended structures around group A1 while they are still visible at 6.7 GHz due to a larger synthesised beam. This would explain the missing flux in the cross-power spectrum for feature A at 12.2 GHz. Group A2, seen at 6.7 GHz only, does not have any detected extended emission, but instead consists of three distinct blobs. Finally, group C at 12.2 GHz represented as two stars in the VLBI centroid map is divided in two distinct masing regions with possible weak emission linking them in the intensity image.

Figure A.2 shows the visibility amplitude vs. uv-distance for several different spectral features. Similarly to the case of G 29.95–0.02, it is possible to roughly estimate the sizes of the masing structures, especially those responsible for the missing flux in the cross-power spectrum. The visibility amplitudes for several channels corresponding to the maximum intensity of features in the 12.2 GHz total power spectrum are fitted with two Gaussian functions. The Gaussian fitting of visibility amplitude for features A and C at 6.7 GHz is also given. The results are shown in Fig. A.2 and Table 4. The three components in A1 (knots 1, 2, 3) have identical structures, i.e. a compact

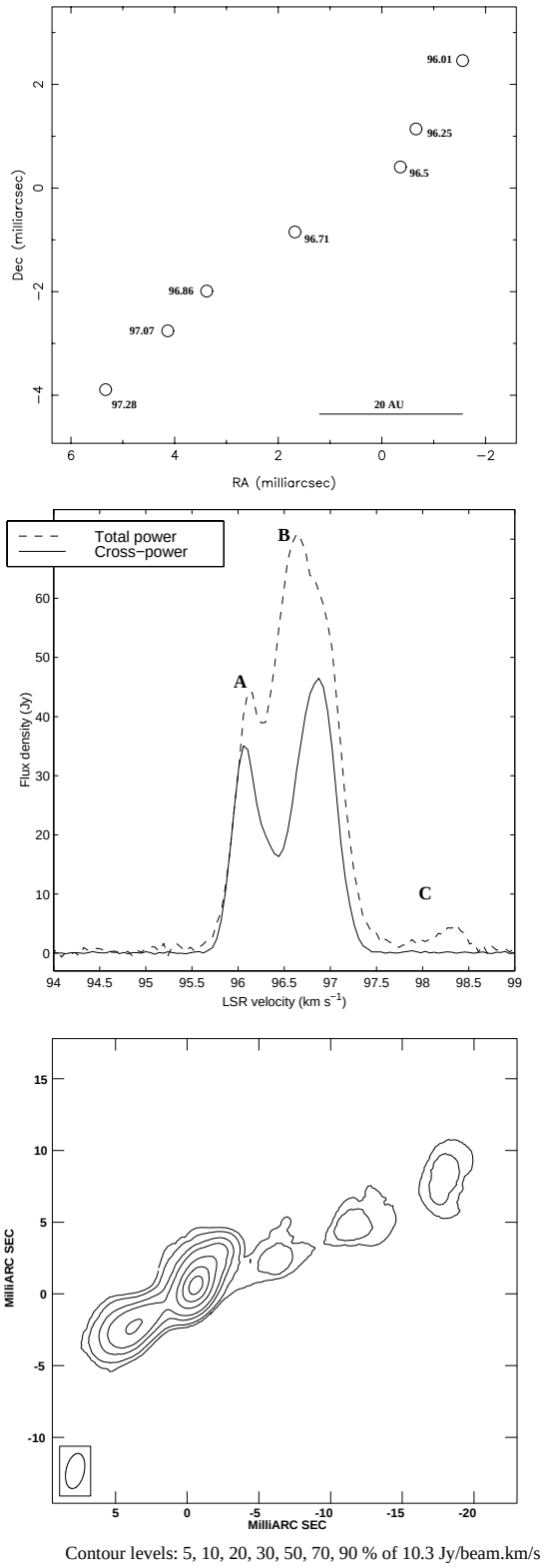

Fig. 1. G 29.95–0.02. Top: VLBA centroid map of the 12.2 GHz methanol maser components (circles). Middle: Cross-power spectrum (solid line) taken on LA-PT and total power spectrum (dashed line) of the 12.2 GHz methanol masers. Bottom: intensity image showing the integrated intensity over the velocity range 95.5–97.5 km s^{-1}. (0, 0) in maps corresponds to the same reference channel position.

core of 3 to 7 AU in extent surrounded by an extended emission of linear dimensions of 12 to 27 AU. The component C also has a similar structure with an extended emission much larger than those in A1. The same results are found at 6.7 and 12.2 GHz for two features seen in both spectra.

2.3. G 9.62+0.20

Figure 3 shows the VLBA centroid map, the methanol maser spectra and the intensity images of several maser components for G 9.62+0.20. The maser components lie in two lines separated by ∼500 AU and are grouped in nine distinct clusters. The clusters appear well separated in the VLBA centroid map. Some groups of masers correspond to different features in the cross-power spectrum. Group F corresponds for example to the spectral features F1 and F2. The correlated flux densities of all the spectral features are reduced compared to their values in the total power spectrum. The flux reduction varies from one spectral feature to another. For instance, features F2, G1, and G2 are only weakly detected on the shortest baselines while E1 and E2 have kept most of their intensity. Additionally, the spectral features are broader in the total power spectrum than in the cross-power spectrum.

Several intensity images are also shown in Fig. 3 for the groups of maser components defined in Paper I. Clearly, the groups A, B, and C form one single structure. Some weak emission links A, B, C and perhaps D into a combined masing region. The intensity image of group D is consistent with the isolated region seen in the VLBA centroid map. However, weak emission detected south of C may connect D with the regions A, B, C. It is also striking that the VLBA resolves A, B and C into a very complicated structure. The reduction of flux of spectral features A, B and C as well as the weak emission detected between the three groups, indicate that some extended emission surrounding these groups is resolved even by the shortest baselines of the VLBA. In contrast to this complex masing region, group E appears in the intensity image with an orientation and dimensions consistent with those in the VLBA centroid map. The flux density of features E1 and E2 corresponding to group E is almost not reduced, suggesting that the image of E shows all the scales of emission in E. Finally, the morphologies of F, H, G and I in the intensity images (Fig. 3) and in the VLBA centroid map are similar.

As for G 29.95–0.02 and NGC 7538, these intensity images strongly suggest the presence of extended emission poorly detected in the map and images, and an estimate of the size of the missing structures can be parameterised by fitting the amplitude visibility of individual spectral channels with two Gaussian functions. Figures A.3 and A.4 show the visibility amplitude vs. *uv*-distance plots for all the features seen in the cross-power spectrum. The results of the Gaussian fitting are given in Table 5. The maser components fall in three classes. The first class consists of

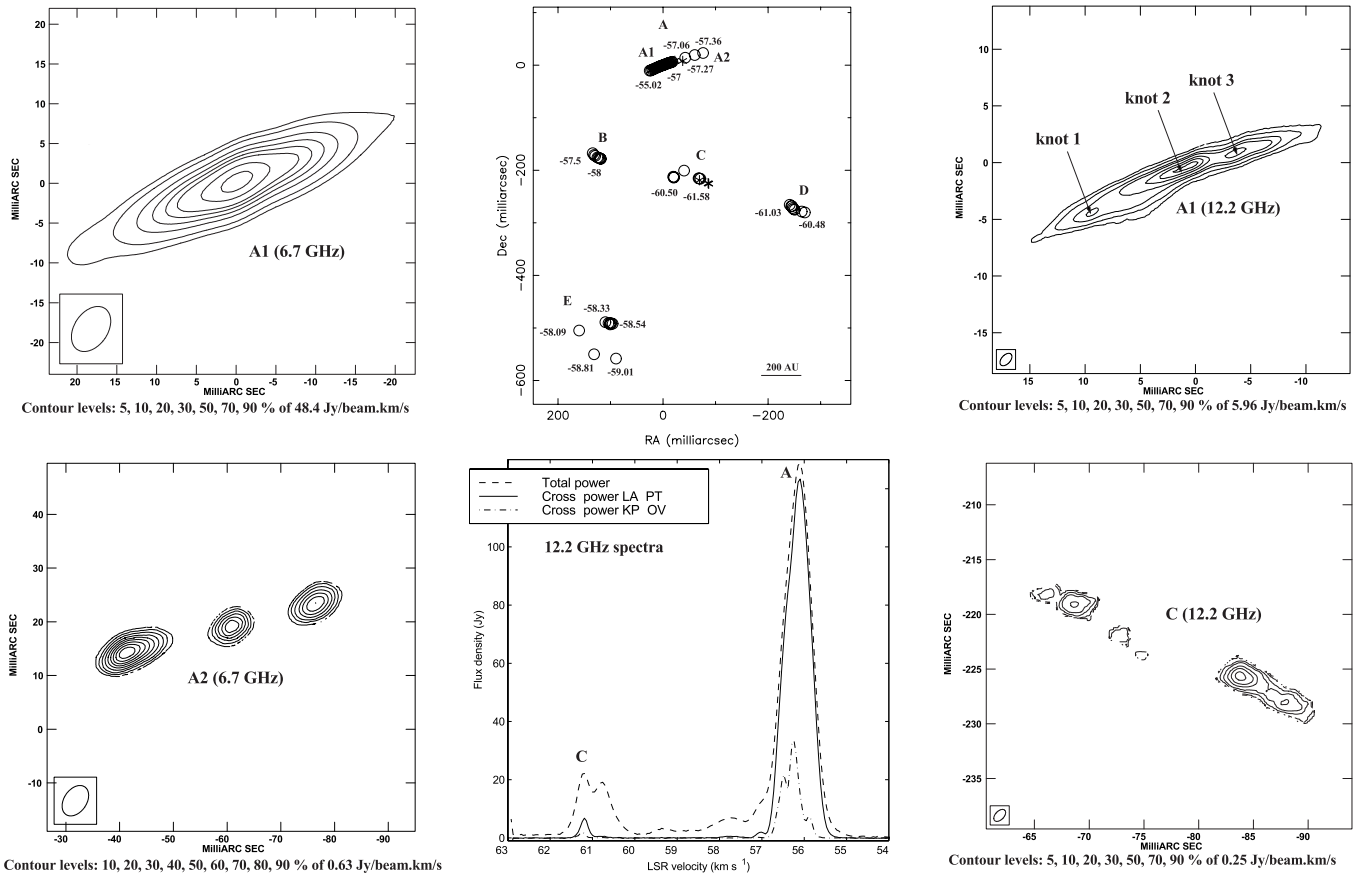

Fig. 2. NGC 7538. Top centre: VLBI centroid map of the 6.7 (circles) and 12.2 GHz methanol maser components (stars) taken from Paper I. Bottom centre: cross-power spectrum taken on LA-PT (solid line) and KP-OV (dashed-dotted line), and total power spectrum (dashed line) of the 12.2 GHz methanol masers. Other plots: intensity images showing the intensity integrated over the velocity width of four spectral features. (0, 0) in maps corresponds to the same reference channel position.

components A, B, C, i.e. spectral features for which the amplitude visibility is reduced progressively with small uv-distance, then decreases more slowly from 20 to 60 Mλ and finally reaches the zero level at the longest baselines. A, B, C are constituted of two structures: a core of ∼20 AU in extent surrounded by extended emission of 50 to 90 AU in extent. The second class of maser components consists of only E1 and E2. Their visibility amplitudes are reduced quickly between 0 and 20 Mλ but are not totally resolved by the longest baselines suggesting both an extended emission and a very compact and bright core of less than 5 AU in extent. The third group of maser components consists of D, F1, F2, G1, G2, H and I. Their visibility amplitudes are first massively resolved at the shortest baseline by a factor 3 to 10, and then the cross correlated flux slowly decreases with uv-distance. For D, F2, G1, G2 and I, this decrease is extremely slow and the flux remains slightly above the noise level. The presence of a core is not clear. These maser components might be constituted of an extremely compact core surrounded by a very large (>170 AU) halo of extended emission.

2.4. Brightness temperatures of 12.2 GHz methanol masers

In previous sections, it has been shown that the methanol masers often arise from structures consisting of a compact core and a large halo of diffuse emission. The brightness temperatures of the masing halos and cores can be calculated and are derived from the amplitude of the Gaussian fits of their visibility amplitudes. The brightness temperatures (T_b) of observed masers in both halos and cores are given in Table 6, and are calculated as follows:

$$T_\mathrm{b}(\mathrm{halo}) = \frac{\lambda^2}{2k}\frac{S_\mathrm{halo}}{\Omega_\mathrm{halo} - \Omega_\mathrm{core}} \quad (1)$$

$$T_\mathrm{b}(\mathrm{core}) = \frac{\lambda^2}{2k}\frac{S_\mathrm{core}}{\Omega_\mathrm{core}}, \quad (2)$$

where S_halo and S_core are respectively V_1 and V_2 in Tables 3–5, and Ω_halo and Ω_core are respectively the solid angles of the halo and core.

The brightness temperatures of the masing cores are greater than those of the masing halos. The brightness temperature of the halo decreases with its diameter

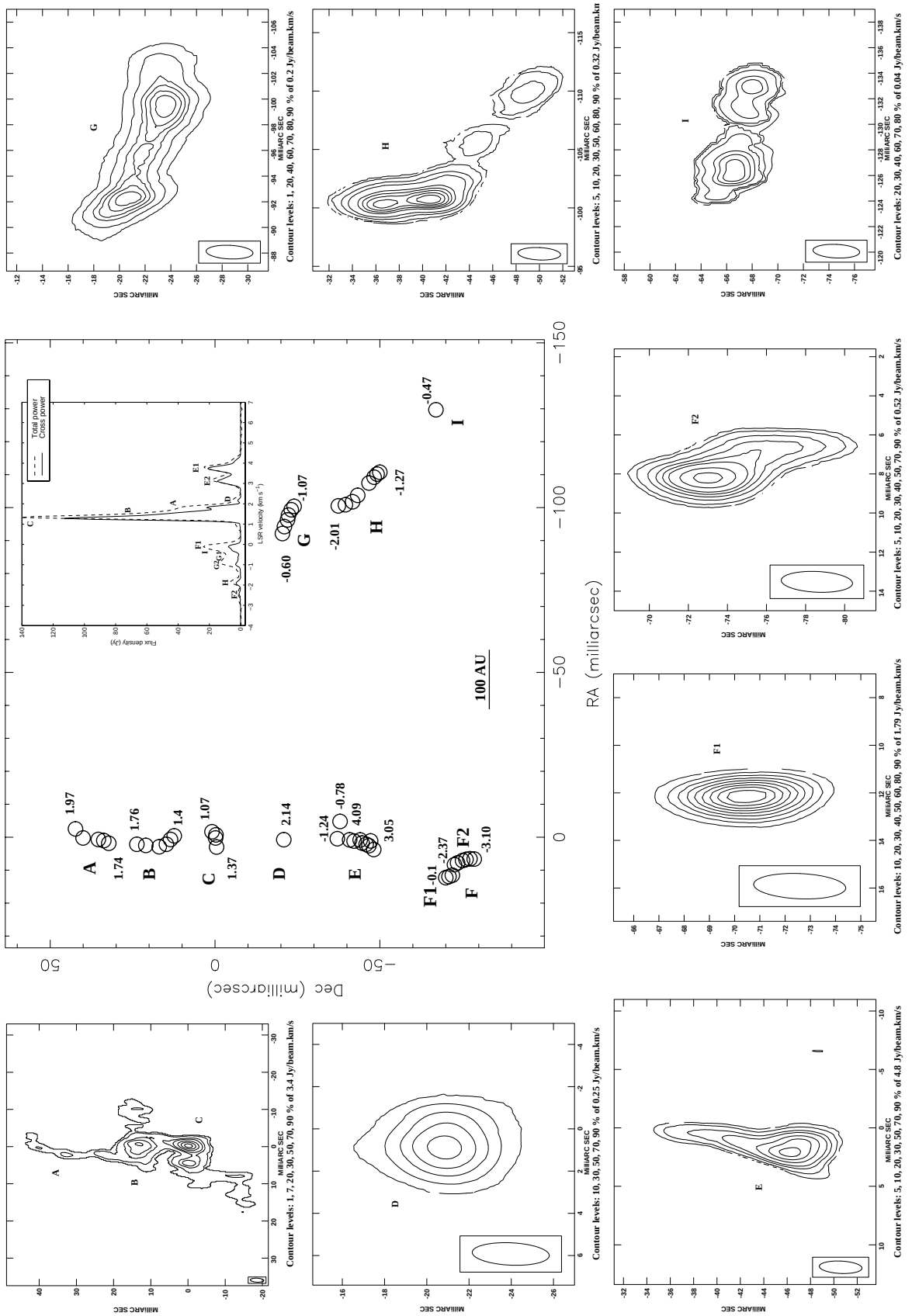

Fig. 3. G 9.62+0.20. Main plot: VLBA centroid map of the 12.2 GHz methanol maser components (circle) taken from Paper I. Inset: cross-power spectrum (solid line) taken on LA-PT and total power spectrum (dashed line) of the 12.2 GHz methanol masers. Close-up: intensity images showing the integrated intensity over the velocity width for each spectral feature. (0, 0) in maps corresponds to the same reference channel position.

Table 3. Parameters of the Gaussian fits of the visibility amplitudes in Fig. A.1 for G 29.95–0.02. The value of the halo diameter derived with only 2 points is given as a lower (>) limit.

Component	Gaussian 1–Halo			Gaussian 2–Core			$\frac{d_1}{d_2}$	$\frac{V_1}{V_2}$	V_1+V_2
	d_1(mas)	d_1(AU)	V_1(Jy)	d_2 (mas)	d_2 (AU)	V_2(Jy)			
A	–	–	–	2.4	18	39	–	–	39
B	>15	>112	40	2.7	20.3	30	5.5	1.3	70

Table 4. Parameters of the Gaussian fits of the visibility amplitudes in Fig. A.2 for NGC 7538.

Component	Gaussian 1–Halo			Gaussian 2–Core			$\frac{d_1}{d_2}$	$\frac{V_1}{V_2}$	V_1+V_2
	d_1(mas)	d_1(AU)	V_1(Jy)	d_2 (mas)	d_2 (AU)	V_2(Jy)			
A1-knot 1	10	27	65	2.3	6.2	35	4.3	1.9	100
A1-knot 2	5	13.5	90	1.2	3.1	35	4.2	2.5	125
A1-knot 3	4.5	12.1	54	1.5	4	18	3	3	72
A1(6.7 GHz)	5	13.5	176	3	8.1	100	1.7	1.8	276
C(12.2 GHz)	25	67.5	15	3.5	9.5	5	7.1	3	20
C(6.7 GHz)	17	45.9	25	5	13.5	18	3.4	1.4	43

Table 5. Parameters of the Gaussian fits of the visibility amplitudes in Figs. A.3 and A.4 for G 9.62+0.20. The values of the halo diameters derived with only 2 points are given as lower (>) limits.

Component	Gaussian 1–Halo			Gaussian 2–Core			$\frac{d_1}{d_2}$	$\frac{V_1}{V_2}$	V_1+V_2
	d_1(mas)	d_1(AU)	V_1(Jy)	d_2 (mas)	d_2 (AU)	V_2(Jy)			
A	15	85.5	32	3	17.1	6	5	5.3	38
B	9	51.3	41	3.5	19.9	9	2.5	4.5	50
C	11	62.7	70	2.8	16	60	3.9	1.2	130
D	>35	>199.5	3.8	1	5.7	1.2	35	3.2	5
E1	6	34.2	8	0.7	4	15	8.6	0.5	23
E2	20	114	6.5	0.75	4.3	11.5	26.7	0.5	18
F1	>30	>171	16.5	1	5.7	7.5	30	2.2	24
F2	>50	>280	–	–	–	–	–	–	–
G1	>50	>285	9	0.5	2.8	1	100	9	10
G2	>40	>228	11	2	11.4	2	20	5.5	5.5
H	>40	>228	4.5	2.4	13.7	2	16.7	2.2	6.5
I	>50	>285	10	0.75	4.3	1	66.7	10	11

(Fig. 4). In contrast, the brightness temperature of the core seems to be less related to the apparent core diameter (Fig. 4). However, the core points fill naturally the upper part of the halo diagram when plotting together the brightness temperatures of cores and halos versus their diameters. A linear fit of $\log T_\mathrm{b}$ vs. $\log d$ for the halo plot in Fig. 4 shows that $T_\mathrm{b} \propto d^{-2.2}$. A similar behaviour of T_b with the apparent size of the maser was found by Emmering & Watson (1994) for the idealised case of uniform spherical masers having similar gas masses and differing only in radius. This result tends to give support to the modelling of methanol masers as uniform spherical masers.

3. Discussion

3.1. Summary of the results

The results described in Sect. 2 can be summarised as follows:

1. For most spectral features, flux density is missing in the cross-power spectra compared to the flux density measured in the total power spectra;
2. The spectral features in the total power spectra are broader than those in the cross-power spectra; and the maximum intensity of a spectral feature in the cross-power spectrum is shifted in velocity with respect to that in the total power spectrum;

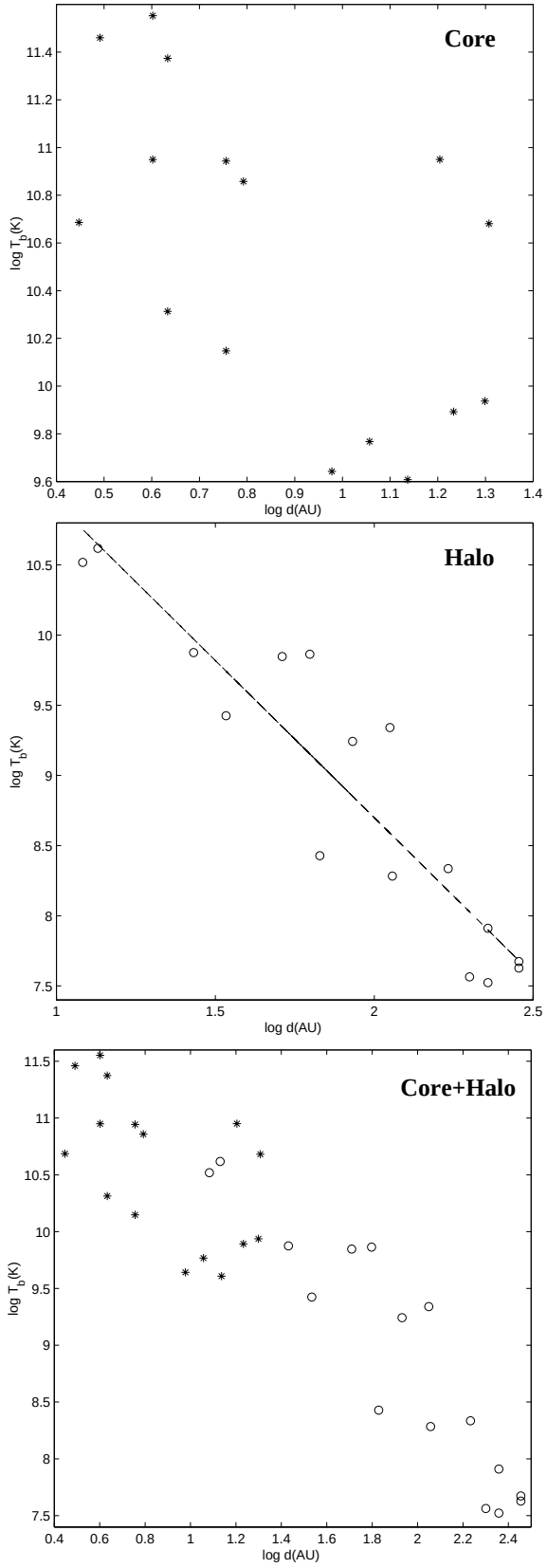

Fig. 4. Top: brightness temperature vs. diameter of the maser core. Middle: brightness temperature vs. diameter of the maser halo. Bottom: brightness temperature vs. diameter of the maser core (stars) and halo (circles).

Table 6. Brightness temperatures of masing halos and cores in G 29.95–0.02, NGC 7538 and G 9.62+0.20. The halo brightness temperature is derived from the parameters of Gaussian 1 while the core brightness temperature is calculated using Gaussian 2 in Tables 3–5.

Source	Component	Halo log T_b(K)	Core log T_b(K)
G 29.95-0.02	A	–	10.9
	B	<9.3	10.7
NGC 7538	A1-knot 1	9.9	10.9
	A1-knot 2	10.6	11.5
	A1-knot 3	10.5	10.9
	C	8.4	9.6
G 9.62+0.20	A	9.2	9.9
	B	9.8	9.9
	C	9.8	10.9
	D	<7.6	10.1
	E1	9.4	11.6
	E2	8.3	11.4
	F1	<8.3	10.9
	F2	–	–
	G1	<7.6	10.7
	G2	<7.9	9.8
	H	<7.5	9.6
	I	<7.7	10.3

3. The VLBI centroid maps, showing the averaged positions over ∼0.2 km s^{-1} of the peak emission in the channel maps, do not give a complete picture of the masing regions;
4. The velocity integrated intensity images show that many maser components are indeed linked by weak emission;
5. The visibility plots suggest that most of the maser components consist of a compact core surrounded by some extended emission or a halo;
6. The compact cores and halos have similar spectral properties, exhibit in many cases similar flux densities and are centred at the same position;
7. Bright masing regions appear to have small halos while weak masing regions have large halos;
8. Some spectral features have no detectable compact core;
9. The properties listed above occur in all three studied sources, and hence are probably intrinsically connected to the maser phenomena and not to the nature of the associated stellar objects.

These results show that extended emission is common in methanol masers. Previous plots of maser regions with dots indicating the centroid of peak emission of velocity components (Paper I) give an incomplete picture. Similar observations of halos for other maser species have been reported in the last years. This phenomenon has been seen in OH megamasers (Diamond et al. 1999), in OH masers in supernova remnants (Claussen et al. 1999), in SiO masers in circumstellar envelopes (Greenhill et al. 1995),

in galactic H_2O masers (Gwinn 1994) and in 25 GHz methanol masers (Sobolev et al. 1998). In addition to these results, Moscadelli et al. (1999) observed in W 3(OH) that a large amount of flux density was missing in the cross-power spectrum of the 12.2 GHz methanol masers. They sketched several possibilities in order to explain the missing flux such as undetected maser features or maser structures resolved out by the shortest baseline.

Several scenarios might explain the structural characteristics of masing regions. **(1)** The core/halo structures are produced by scattering effects and do not reflect the physical size of the maser source. **(2)** The core/halo structures are due to saturation effects in a uniform spherical maser cloud. **(3)** The extended emission originates in distinct masing regions with different physical conditions. The cores would be very dense and abundant in methanol while the halo would be diffuse gas. **(4)** Turbulence could disrupt a homogeneous medium into clumps with a core/halo appearance. These possible explanations are discussed in the next sections.

3.2. Scattering effects

Scattering effects can often play a role in the broadening of the maser images as argued by Moran et al. (1973) for OH and H_2O masers in W49N. They found that "the ratio of the size of the smallest OH masers to that of the smallest H_2O masers was nearly equal the ratio of the squares of the wavelengths". Such a result is expected for scattering broadening that varies as λ^2 (i.e. scattering by a screen with a Gaussian correlation function; Rickett 1977) or as $\lambda^{2.2}$ (i.e. scattering by interstellar irregularities with a standard Kolmogorov spectrum; Rickett 1977; Blandford & Narayan 1985). The consequence of this phenomenon produced by ionised gas along the line of sight to the maser source was further studied by Cordes et al. (1991). They defined the scattering measure to characterise the strength of interstellar scattering within the Galaxy as $SM = (\theta_S/71\,\mathrm{mas})^{5/3}{\nu_{\mathrm{GHz}}}^{11/3}$ for Galactic sources where ν_{GHz} is the observing frequency and θ_S is the angular broadening of the image.

Since all the methanol sources lie close to the Galactic plane, some degree of scattering broadening is expected. This could explain the apparent presence of extended emission. One can check this hypothesis by estimating the apparent size of the maser due to scattering effects using the formulae in Cordes et al. A maximum value of SM equal to 1 kpc $\mathrm{m}^{-20/3}$ for Galactic sources (see Cordes et al.) gives a maximum value of θ_S equal to 0.3 mas at 12.2 GHz and 1 mas at 6.7 GHz. The measured values of θ_S for the methanol maser halos at 12.2 GHz vary between 5 and 50 mas and are therefore unlikely to be produced by interstellar scattering. Conversely, the measured angular sizes of the maser halos would require SM between 100 and 5000 kpc $\mathrm{m}^{-20/3}$. This highly enhanced scattering could originate from the immediate vicinity of the maser site. Gwinn (1994) suggested this explanation to model the galactic H_2O maser halos in W 49N. The 12.2 GHz methanol masers are located near massive young stellar objects (Paper II) which are surrounded by optically thick and ionised gas regions such as ultra-compact H II regions (UC H II). The optical depth of such regions in the case of detected UC H II regions is greater than 1 when the frequency is lower than 13 GHz (Churchwell 1991). Therefore, emission at 6.7 and 12.2 GHz will be affected by the optically thick regime of the ionised gas region. However, scattering effects are expected to be frequency dependent. For NGC 7538, values of the angular broadening have been derived at both 6.7 and 12.2 GHz for features A1 and C. The ratio of the halo angular sizes for A1 and C at 12.2 GHz and 6.7 GHz are respectively 1 and 1.5. Using $\theta_S \propto \nu^{-2.2}$, a ratio of 0.27 would be expected if scattering by interstellar irregularities dominates. The maser angular broadening is therefore almost independent of the observing frequency. Additionally, some extended masers do not have a compact core and cannot be explained by scattering effects as modelled by Gwinn (1994) for the case of H_2O masers. These two arguments show that scattering effects are not responsible for the large halos of extended emission.

3.3. Saturated spherical masers

Saturation effects are intrinsically connected to maser action. They provide a self-limiting mechanism to the exponential growth of the maser intensity. Saturation effects are also responsible for changes in the beaming effects which modify the appearance of masers as seen by an observer (Elitzur 1990a, 1990b).

For a uniform sphere of gas with uniform pumping conditions throughout, three different maser structures can form depending on the efficiency to convert each pumping event into one maser event. As this conversion efficiency converges to 1, the maser goes from a totally unsaturated stage, to one with a partially saturated outer layer, to finally one which is saturated throughout. Below we describe these three different maser stages and the expected appearance of the spherical masers in each case.

(1) Fully unsaturated: first an incident radiation increases exponentially as it propagates within the unsaturated spherical maser. The ray travelling along the longest distance (i.e. a diameter) is the most amplified while the masers originating from shorter path lengths are much weaker. As a result, the maser is beamed in the radial direction (Fig. 5a).

(2) Partially saturated: as the maser intensity (I_ν) grows with the travelled distance, it reaches a saturation limit (I_s) in the regions outside the centre of the sphere and the spherical maser is divided in two zones (Fig. 5b): an unsaturated core and a saturated shell. The dominant rays (i.e. those passing through the centre of the sphere) compete for induced photons with the ray originating in the saturated shell at every position in the saturated zone (P in Fig. 5b). The subordinate rays carry an intensity

much smaller than I_s. Since a stimulated photon moves into the same direction as the stimulating photons and the probability ($\propto B_{21}I_\nu$) for the emission of stimulated photons is higher for the dominant ray than for any other rays, only the radiation of dominant rays will grow within the saturated shell. This implies an even tighter beaming of radiation than in the unsaturated core whose expression is given by Elitzur (1990b):

$$\Omega_B \simeq \frac{\pi r_c}{-k_{0\nu}R^2} \quad (3)$$

where r_c is the core radius, R is the spherical maser radius and $k_{0\nu} = -\Delta P B_{21} h\nu\phi(\nu)/4\pi\Gamma$ is the absorption coefficient in the unsaturated zone; ΔP is the difference between the pumping rates per unit volume to the upper and lower maser levels; Γ is the rate loss; $\phi(\nu)$ is the emission line profile function; and B_{21} is the Einstein coefficient for stimulated emission.

(3) Fully saturated: as the saturated shell expands, the unsaturated core shrinks logarithmically with R until I_ν at the centre of the sphere is equal to I_s. Core saturation occurs when $-k_{0\nu}r_c \leq 2.15$ (Elitzur 1990b). Once the core has fully saturated, it disappears within a fully saturated maser sphere. The beaming angle is now constant and much larger than in stages 1 and 2. The maser intensity varies linearly with the distance along the ray through the sphere.

Our data reveal core/halo structures as sketched in Fig. 5c. The measured brightness temperatures (see Table 6) indicate that the cores are much brighter than the halos. These results are expected when observing a partially saturated spherical maser as explained in Fig. 5b. It is therefore tempting to speculate that the measured core/halo structures are the apparent images produced by unsaturated cores surrounded by saturated shells. Note that in such a model, the emission from the *observed* bright maser core is not exactly the emission from the *unsaturated* maser core, but is the result of beaming effects, exponential growth in the unsaturated zone and saturation in front of the unsaturated core (Fig. 5c). The emission from the *deduced* maser halo is weak maser from the edges of the *saturated* maser shell, i.e. weak emission that does not pass through the unsaturated core (Fig. 5c).

These hypotheses can be tested by applying analytical solutions for spherical masers from Elitzur (1990b) to our data. In the following calculations, two assumptions will be made and are illustrated by Fig. 5c. **(1)** All radiation passing through the unsaturated core is detected. **(2)** Weak radiation passing through the shell is partially detected. These assumptions require $r_c = d_2/2$, $r_c < R$ and $d_1/2 < R$ to be self-consistent.

In a spherical maser, the beaming angle is defined by the ratio of the apparent radius to the radius of the sphere (Fig. 5c). Hence, the solid beaming angle is the ratio to the power two of the core diameter (d_2) to the spherical maser diameter ($2R$) times π:

$$\Omega_B = \pi \frac{{d_2}^2}{(2R)^2} \quad (4)$$

where d_2 is from Tables 3–5. The product $-k_{0\nu}r_c$ can also be estimated from the observational data and is calculated using Eq. (3) and the following expression:

$$k_{0\nu} = \frac{-3D^2 F_{obs}}{4\pi J_s R^3} \quad (5)$$

where D is the distance to the source, F_{obs} is the measured flux density and $J_s = \Gamma/2B_{21}$. The above equation is deduced from the total maser luminosity $L_\nu = -4\pi k_{0\nu} J_s V = 4\pi D^2 F_{obs}$, V being the maser volume (Elitzur 1990b). Ω_B, R, $-k_{0\nu}$ and r_c are calculated by solving Eqs. (3)–(5) together with $r_c = d_2/2$. Their values are given in Table 7. From Eqs. (3) and (4) and $r_c = d_2/2$, $-k_{0\nu}r_c = 1$ is deduced that should be compared to 2.15 for the case of saturation within the core (Elitzur 1990b). In consequence, since $-k_{0\nu}r_c$ is below this critical value, our assumptions imply saturation even within the core. The ratio of T_b(core) to T_s is given in Table 7 where T_s is the brightness temperature at which the maser saturates:

$$T_s = \frac{\lambda^2}{2k}\frac{4\pi}{\Omega_B}\frac{\Gamma}{2B_{21}}. \quad (6)$$

Taking the rate loss $\Gamma = 0.6\ s^{-1}$ (Sobolev priv. comm. and Sobolev et al. 1997b) and $B_{21} = 3 \times 10^{11}$ m^2 Hz sr J^{-1} (using $A_{21} = 8 \times 10^{-9}\ s^{-1}$ in Lees 1973), the masers are saturated when $T_b > T_s$. All the masers are saturated as $\log[T_b(\text{core})/T_s] > 0$ in Table 7. Finally, the ratio of r_c to R is given in Table 7 to check the self-consistency of the hypotheses since r_c should satisfy $d_2/2 \leq r_c < R$ (see Fig. 5d).

Column 10 in Table 7 gives the ratio (K) of the halo radius ($d_1/2$) to the derived radius of the spherical maser clouds (R). K varies from 0.2 to 8.6. More precisely, K is in the range [0.2; 0.8] for eight components and in the range [1.3; 8.6] for another eight components. All of the latter case except one occur in the source G 9.62+0.20. $K < 1$ means that d_1 underestimates the sizes of the spherical maser clouds. This is likely since the weakest masers from the edges of the shell are not expected to be detected. Overestimate of halo sizes ($K > 1$) is also expected if the single dish flux density (i.e. the zero-spacing visibility value in Figs. A.1–A.4) is overestimated. In addition, the halo sizes for $K > 1$ are derived from Gaussian fitting with two or three points (e.g. F1 in G 9.62+0.20; Fig. A.4). Errors in both amplitude calibration and Gaussian fitting could explain our results. Finally, the spherical geometry may be too idealised for modelling the maser structures. This is probably true for the components with $K > 1$ in G 9.62+0.20. A more complex geometry (e.g. cylindrical maser geometry) is probably required.

In conclusion, saturation could explain the core/halo structures, but this model would imply in many cases large errors on the estimate of the halo diameters. Forthcoming MERLIN+EVN observations with shorter baselines might solve this puzzle.

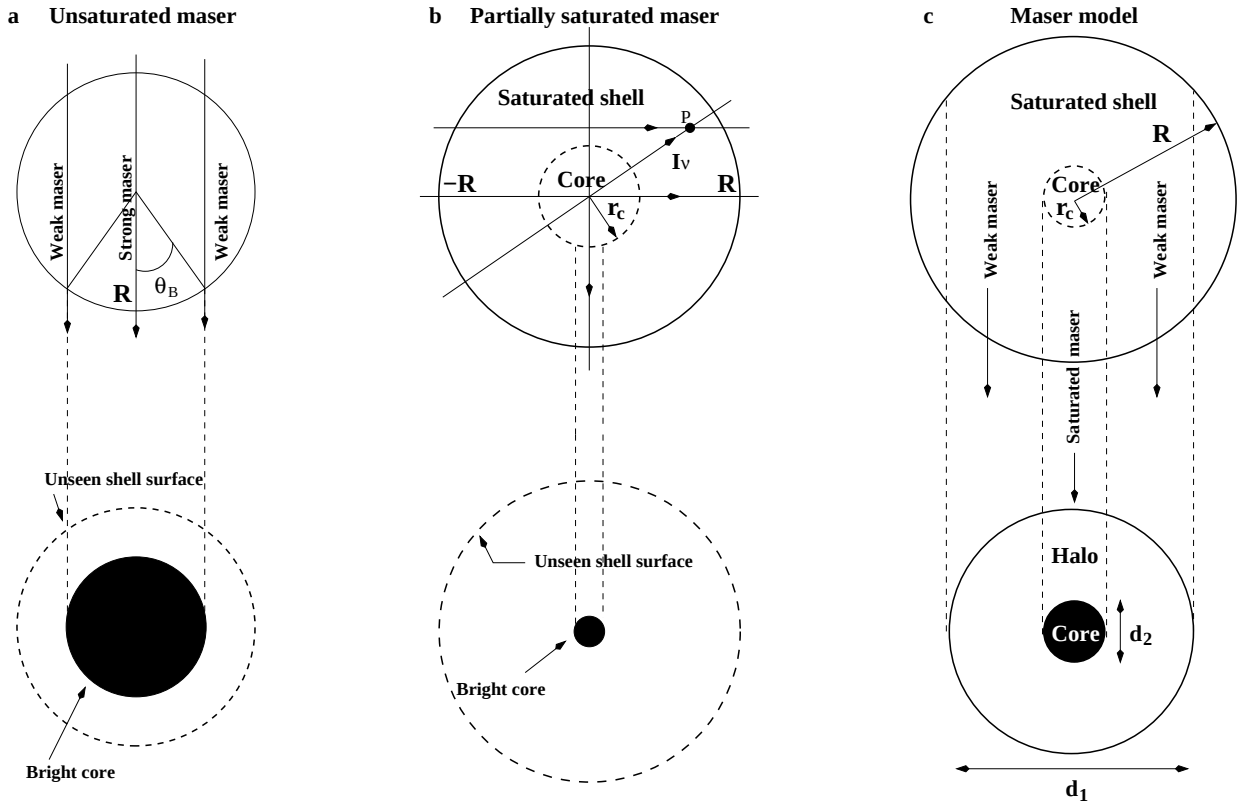

Fig. 5. a) Unsaturated spherical maser. Beaming effects are due to the rapid decrease of the surface intensity with θ. An observer would see a bright core with an apparent diameter equal to $R\theta_B$. **b)** Partially saturated spherical maser consisting of an unsaturated core and a saturated shell. An observer would see a smaller bright core in case of strong beaming effects. **c)** Model of the observed methanol masers. We might observe partially saturated spherical masers consisting of a bright core surrounded by a possible halo of weak emission. The halo diameter is deduced from the visibility plots. The bright maser core is produced by radiation along the dominant ray, i.e. a radiation that exponentially grows in the unsaturated core, and then saturates in the saturated shell. The halo emission is provided by weak radiation that does not go through the core.

3.4. High density "pockets" of methanol in shocks and disks

The comparison of the total power spectra with the cross-power spectra indicates that some weak features are totally resolved out by the shortest baselines. For example, feature C in G 29.95–0.02 and some emission between −58 and −61 km s^{-1} in NGC 7538 have almost disappeared in the cross-power spectra. Their corresponding maser components cannot be found in the VLBI channel map despite a noise level below 50 mJy/beam for the weakest emission. The visibility amplitude of these spectral features remains at the noise level found in all the other visibility plots. Thus, these masing regions exhibit only extended emission in contrast to the majority of the maser components showing both a bright core and extended structures. This observation suggests that the extended masers arise from physically extended regions not necessarily associated with a compact masing core. Therefore, the halo and core masers could originate in distinct regions.

If diffuse emission was really caused by a collection of weak masers spreading over large physical regions, the large regions of masing gas should correspond in position to large clumps of gas detected using traditional tracers. Such a correspondence is observed in NGC 7538–IRS1 (Paper II). In that star-forming region, each methanol maser clump within the south part of the outflow is coincident with an emission clump of ionised gas. Gaume et al. (1995) have argued that the resolved emission clumps seen at 22 GHz trace "pockets" of molecular gas ionised by the young massive star. The extent of these pockets is about 200 AU which is much larger than the average maser core size (10 AU); on the other hand, the ionised clump sizes are roughly equal to the estimated halo diameters. Hence, the maser cores could trace high density cores at the centre of the gas pockets while the halo masers could originate in less dense gas with lower column densities.

More precisely, it has been shown in Paper II that methanol masers originate in shocks associated with ionised jets and in protostellar disks. Then, in a shock the maser could form in pockets of gas shocked by the passage of fast shock waves. The maser halos would form in residual diffuse gas taken away by the shock wave along large distance as seen in the ionised stellar outflow in NGC 7538 (see Fig. 2 in Paper II). Similarly, in a disk the densest gas clouds could be large condensations of icy dust grains that melt progressively. The methanol gas abundance increases around the condensation. As the condensations

Table 7. Maser quantities derived from the observational data. $2R$ is in AU. T_b values are the core brightness temperature taken from Table 6. $K = d1/2R$.

Source	Comp.	$\log\Omega_B$	$2R$	$\log\frac{T_\mathrm{b}}{T_\mathrm{s}}$	$\log\frac{r_\mathrm{c}}{R}$	K
G29.95	A	–	–	–	–	–
−0.02	B	−1.65	240.1	0.60	−1.07	0.5
NGC7538	A1-k1	−1.77	84.0	0.65	−1.13	0.3
	A1-k2	−2.17	66.7	0.85	−1.33	0.2
	A1-k3	−1.83	58.1	0.68	−1.16	0.2
	C	−0.96	50.6	0.25	−0.72	1.3
G9.62	A	−1.12	110.4	0.33	−0.81	0.8
+0.20	B	−1.15	133.0	0.35	−0.82	0.4
	C	−1.83	232.7	0.69	−1.16	0.3
	D	−1.29	44.8	0.42	−0.89	4.4
	E1	−2.23	92.3	0.89	−1.36	0.4
	E2	−2.11	86.6	0.83	−1.30	1.3
	F1	−1.82	82.5	0.68	−1.16	2.1
	F2	–	–	–	–	–
	G1	−1.65	33.2	0.60	−1.07	8.6
	G2	−1.04	66.9	0.29	−0.77	3.4
	H	−0.93	71.1	0.24	−0.71	3.1
	I	−1.40	38.3	0.47	−0.95	7.5

rotate around the massive star, due to the viscosity the methanol gas rotates slower than the condensation and remains in orbit to finally form a tail of diffuse gas. The images of masers within a disk would appear as some strong masers surrounded by diffuse emission (Fig. 2) located in front of the star where the velocity coherence is highest as seen in NGC 7538 (Paper I). Obviously, this model is not specific to methanol and could potentially apply to other species with maser capabilities evaporating from the icy dust mantles. NH_3 belongs to such a group of species. It is interesting to note that NH_3 masers were detected in NGC 7538 and coincide in position with two methanol maser clumps (Minier et al. 1998).

The existence of physically extended masers is a very important issue regarding the nature and the overall size of the masing regions. For instance, if the extended emission arises from large physical regions having the same position angle as the maser spot structure, the sizes of the linear structures of masers reported in Paper I are a lower limit of their true lengths (Case 1 in Fig. 6). In Paper I, it was argued that the lines of masers delineate partially edge-on disks. Therefore, the measured extent of the maser lines is a lower limit of the radius (r) of the edge-on disk. Since the Keplerian mass is proportional to r^3, a total extent larger than measured in the VLBI centroid map (i.e. in Paper I) will imply higher central masses. Conversely, undetectable extended emission could have a position angle totally different to that of the structure seen using the maser spot approach and rule out the disk hypothesis

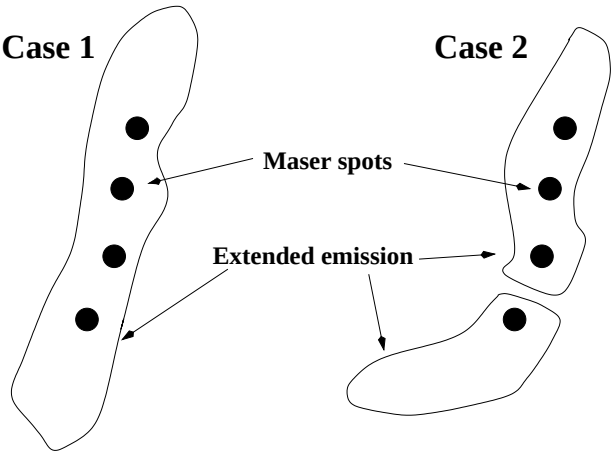

Fig. 6. Illustration comparing two different geometries for diffuse emission in relation to the compact maser cores. Case 1: the extended emission has the same position angle as that of the maser spot structure. Case 2: the extended regions of diffuse emission associated with different maser components do not confirm the overall maser spot structures.

(Case 2 in Fig. 6). Then, recovering the extended emission would give information about the origin of methanol masers, i.e. disks or shocks.

3.5. Turbulence

Velocity fields including turbulent velocity could disrupt the image of a homogeneous methanol gas region into an apparent clumpy medium in velocity exhibiting masers. Since maser phenomena depend critically on the velocity coherence along the line of sight, the additional field of turbulent velocity could recreate velocity coherence at any position. In such a medium, the observed sizes of halos and cores are not the physical sizes of dense and hot regions exhibiting masers. Instead, the apparent structures of masing regions are shaped by the turbulent velocity field as suggested by the images of 25 GHz methanol maser clumps modelled by Sobolev et al. (1998). They have also shown that intense spectral features correspond to small apparent masing regions in the maps. This latest result is observed in our data (item 7 in Sect. 3.1). This turbulence could explain the clumpy structure of masing regions as well as their spectral profile properties described in item 2 (Sect. 3.1).

4. Summary and conclusions

We have collected evidence suggesting that extended emission is resolved even by the shortest baselines of the VLBA, and that extended emission is responsible for the missing flux density in the cross-power spectra of methanol masers. The majority of the masing regions consist of a compact core surrounded by a halo of emission.

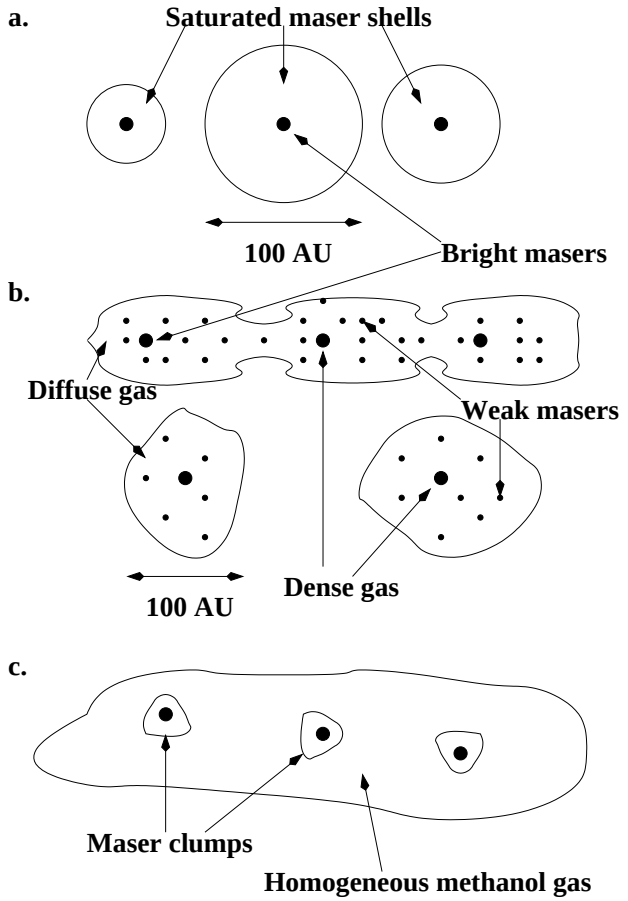

Fig. 7. Illustration summarising the possible phenomena explaining the core/halo structures. **a)** Saturated spherical masers. **b)** High density pockets of methanol in disks and shocks. **c)** Turbulence in a homogeneous methanol gas.

Different phenomena could explain the presence of large-scale emission (see Fig. 7 for illustrated summary):

1. Scattering effects do not play a role in the broadening of maser images since masers have similar sizes at 6.7 and 12.2 GHz.
2. Saturation may explain the core/halo structure for a few maser features. However, modelling the core/halo structure as saturated spherical masers implies large errors on the size of the halos.
3. The large masing regions and the compact masing regions form in physically distinct regions. The core would trace high density conditions while the halos would be the result of weak and diffuse masers.
4. Turbulence in an homogeneous medium could create suitable velocity conditions to form maser core/halo structures. But the physical mechanism supporting turbulence is uncertain.

Further interferometric observations included shorter baselines are needed to recover and image the resolved structures, and thus differentiate between the three possible scenarios.

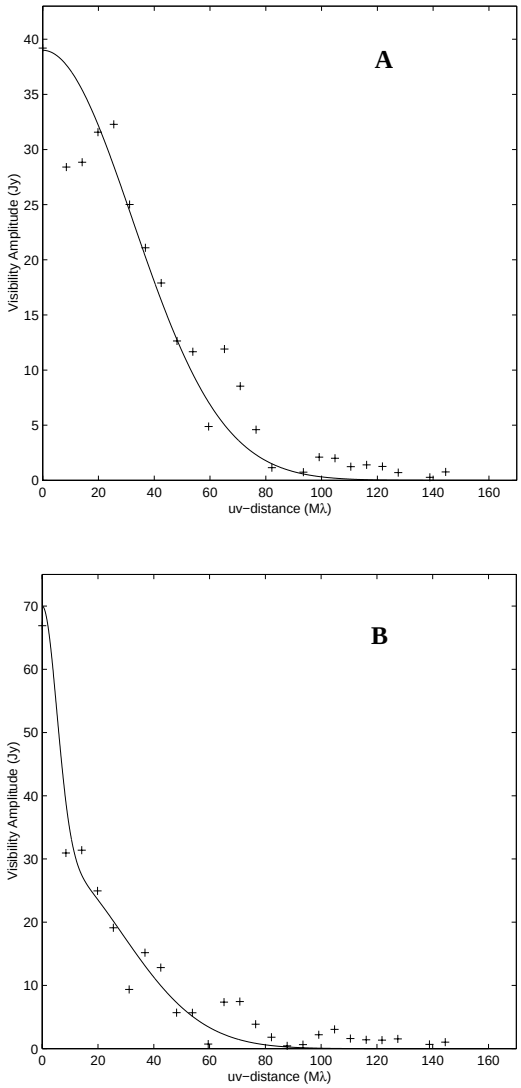

Fig. A.1. G 29.95–0.02: visibility amplitude vs. *uv*-distance for components A, B defined in Fig. 1. Each cross gives the value of the binned visibility amplitude. Note that noise biasing has been removed by estimating the noise level in channels without any maser feature.

Appendix A: Visibility plots

In this appendix, the visibility vs. *uv*-distance plots are presented for the channels corresponding to the peak intensity of every spectral features in the three methanol maser spectra taken toward G 29.95–0.02, NGC 7538 and G 9.62+0.20. The labels given on the plots correspond to those given in the related spectra and VLBI maps.

Acknowledgements. We thank the VLBA and EVN stations for their assistance during our VLBI observations. We also thank Andrej Sobolev and Andrei Ostrovskii for valuable comments and communicating us the value of the methanol maser loss rate.

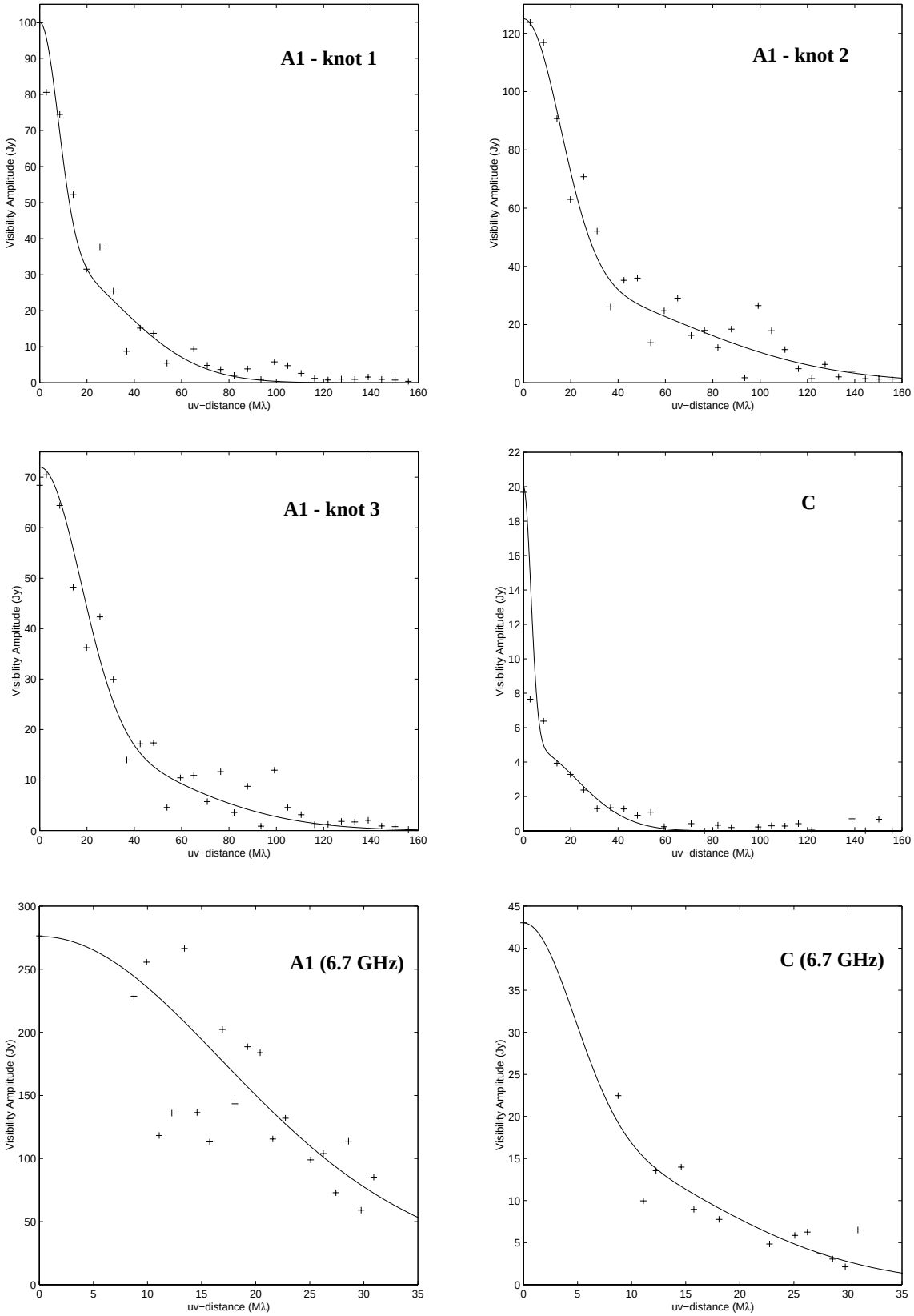

Fig. A.2. NGC 7538: visibility amplitude vs. *uv*-distance for components A1, C at 12.2 GHz defined in Fig. 2. Visibility amplitude vs. *uv*-distance for components A1 and C at 6.7 GHz. Each cross gives the value of the binned visibility amplitude. Note that noise biasing has been removed by estimating the noise level in channels without any maser feature.

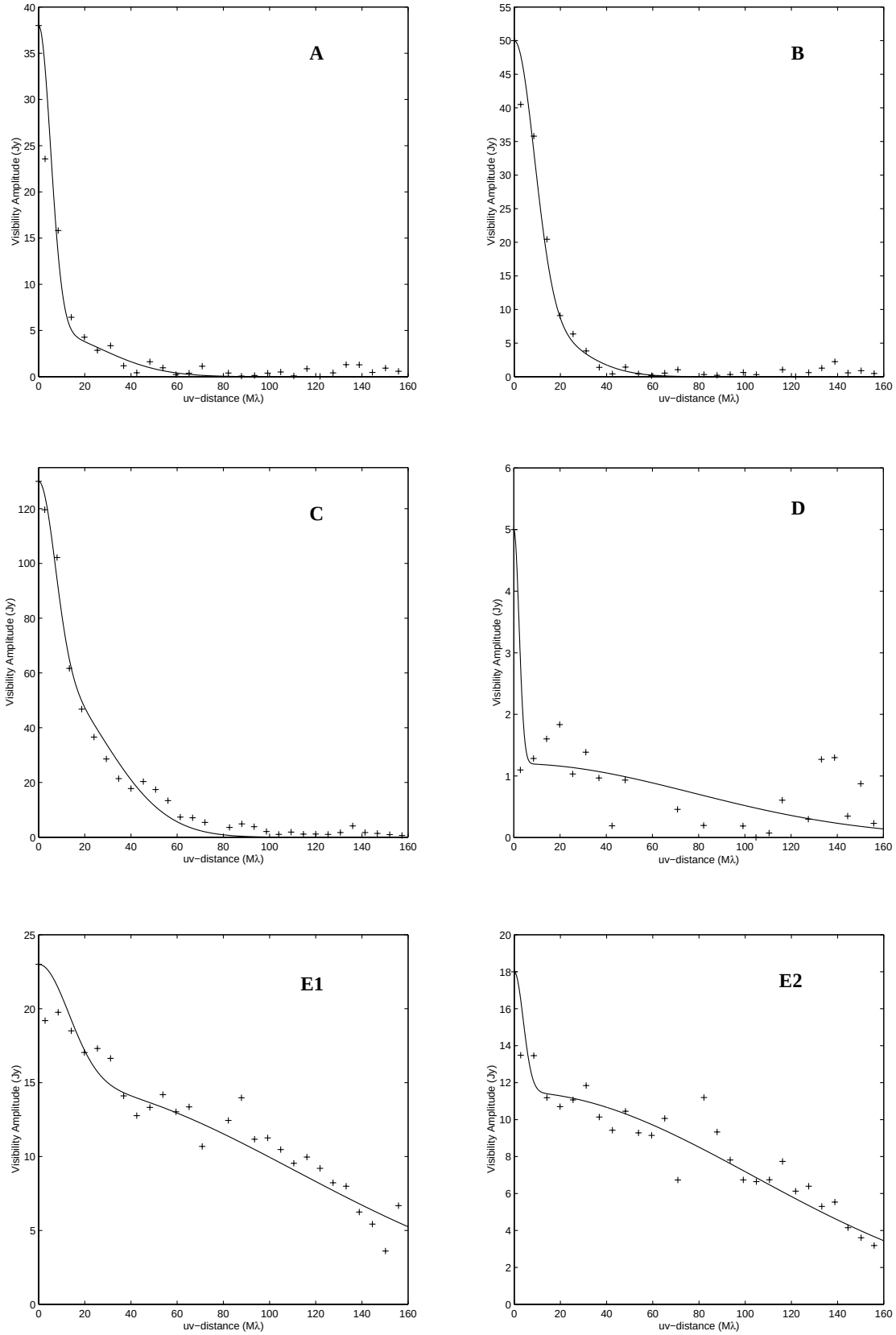

Fig. A.3. G 9.62+0.20: visibility amplitude vs. *uv*-distance for components A, B, C, D, E1, E2 defined in Fig. 3. Each cross gives the value of the binned visibility amplitude. Note that noise biasing has been removed by estimating the noise level in channels without any maser feature.

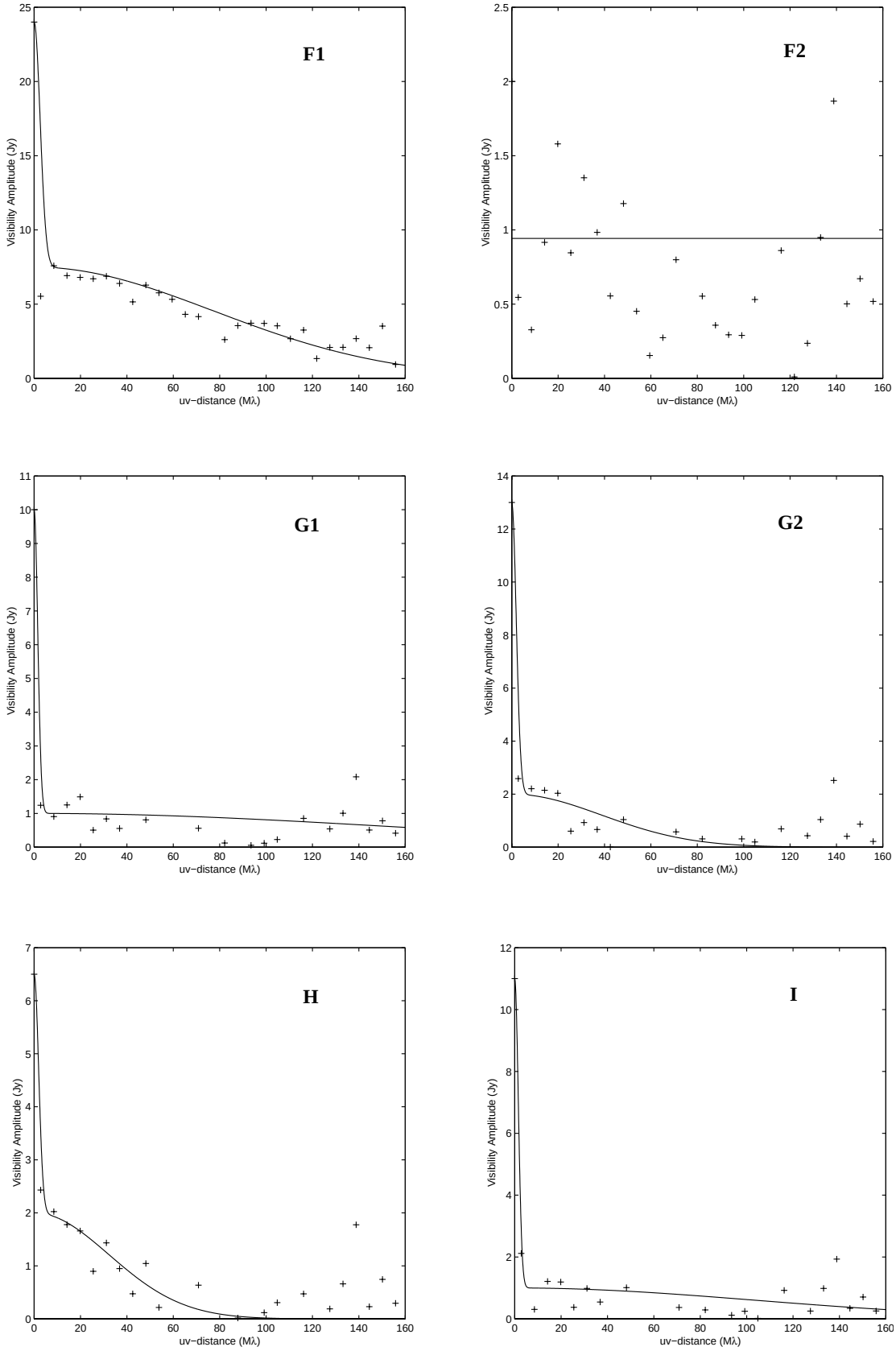

Fig. A.4. G 9.62+0.20: visibility amplitude vs. *uv*-distance for components F1, F2, G1, G2, H, I defined in Fig. 3. Each cross gives the value of the binned visibility amplitude. Note that noise biasing has been removed by estimating the noise level in channels without any maser feature.

References

Blandford, R., & Narayan, R. 1985, MNRAS, 213, 591
Caswell, J. L., Vaile, R. A., & Ellingsen, S. P. 1995a, PASA, 12, 37
Caswell, J. L., Vaile, R. A., Ellingsen, S. P., Whiteoak, J. B., & Norris, R. P. 1995b, MNRAS, 272, 96
Churchwell, E. 1991, in The Physics of Star Formation and Early Stellar Evolution, ed. C. J. Lada, & N. D. Kylafis (Kluwer Academic Publishers), 221
Claussen, M. J., Goss, W. M., Frail, D. A., & Desai, K. 1999, ApJ, 522, 349
Cordes, J. M., Weisberg, J. M., Frail, D. A., & Ryan, M. 1991, Nature, 354, 121
Diamond, P. J., Lonsdale, Co. J., Lonsdale, Ca. J., & Smith, H. E. 1999, ApJ, 511, 178
Elitzur, M. 1990a, ApJ, 363, 628
Elitzur, M. 1990b, ApJ, 363, 638
Emmering, R. T., & Watson, W. D. 1994, ApJ, 424, 991
Gaume, R. A., Goss, W. M., Dickel, H. R., et al. 1995, ApJ, 438, 776
Greenhill, L. J., Colomer, F., Moran, J. M., et al. 1995, ApJ, 449, 365
Gwinn, C. R. 1994, ApJ, 431, L123
Koo, B.-C., Williams, D. R., Heiles, C., et al. 1988, ApJ, 326, 931
Lees, R. M. 1973, ApJ, 184, 763
Menten, K. M., Reid, M. J., Moran, J. M., et al. 1988, ApJ, 333, L83
Menten, K. M., Reid, M. J., Pratap, P., & Moran, J. M. 1992, ApJ, 401, L39
Minier, V., Booth, R. S., & Conway, J. E. 1998, A&A, 336, L5
Minier, V., Booth, R. S., & Conway, J. E. 2000, A&A, 362, 1093 (Paper I)
Minier, V., Conway, J. E., & Booth, R. S. 2001, A&A, 369, 278 (Paper II)
Moran, J. M., Papadopoulos, G. D., Burke, B. F., et al. 1973, ApJ, 185, 535
Moscadelli, L., Menten, K. M., Walmsley, C. M., & Reid, M. J. 1999, ApJ, 519, 244
Rickett, B. J. 1977, ARA&A, 15, 479
Sobolev, A. M., Cragg, D. M., & Godfrey, P. D. 1997a, A&A, 324, 211
Sobolev, A. M., Cragg, D. M., & Godfrey, P. D. 1997b, MNRAS, 288, L39
Sobolev, A. M., Wallin, B. K., & Watson, W. D. 1998, ApJ, 498, 763